

Article

Green Synthesis of TiO₂ Nanoparticles Using *Acorus calamus* Leaf Extract and Evaluating Its Photocatalytic and In Vitro Antimicrobial Activity

Afzal Ansari ^{1,*}, Vasi Uddin Siddiqui ¹, Wahid Ul Rehman ², Md. Khursheed Akram ³, Weqar Ahmad Siddiqi ^{1,*}, Abeer M. Alosaimi ⁴, Mahmoud A. Hussein ^{5,6} and Mohd Rafatullah ^{7,*}

- ¹ Department of Applied Sciences and Humanities, Faculty of Engineering and Technology, Jamia Millia Islamia, New Delhi 110025, India; vasi168968@st.jmi.ac.in
- ² Molecular Genetics Laboratory, Department of Botany, Central University of Punjab, Bathinda 151401, India; wahidulrehman@gmail.com
- ³ Applied Sciences and Humanities Section, Faculty of Engineering and Technology, University Polytechnic, Jamia Millia Islamia, New Delhi 110025, India; makram@jmi.ac.in
- ⁴ Department of Chemistry, Faculty of Science, Taif University, P.O. Box 11099, Taif 21944, Saudi Arabia; a.alosaimi@tu.edu.sa
- ⁵ Chemistry Department, Faculty of Science, King Abdulaziz University, P.O. Box 80203, Jeddah 21589, Saudi Arabia; maabdo@kau.edu.sa
- ⁶ Chemistry Department, Faculty of Science, Assiut University, Assiut 71516, Egypt
- ⁷ Division of Environmental Technology, School of Industrial Technology, Universiti Sains Malaysia, Penang 11800, Malaysia
- * Correspondence: afzal168969@st.jmi.ac.in (A.A.); wsiddiqui@jmi.ac.in (W.A.S.); mrafatullah@usm.my (M.R.)



Citation: Ansari, A.; Siddiqui, V.U.; Rehman, W.U.; Akram, M.K.; Siddiqi, W.A.; Alosaimi, A.M.; Hussein, M.A.; Rafatullah, M. Green Synthesis of TiO₂ Nanoparticles Using *Acorus calamus* Leaf Extract and Evaluating Its Photocatalytic and In Vitro Antimicrobial Activity. *Catalysts* **2022**, *12*, 181. <https://doi.org/10.3390/catal12020181>

Academic Editors: Daria Camilla Boffito, Carlos Escudero-Oñate, Carlo Pirola and Maria Laura Tummino

Received: 28 November 2021

Accepted: 26 January 2022

Published: 30 January 2022

Corrected: 17 November 2022

Publisher's Note: MDPI stays neutral with regard to jurisdictional claims in published maps and institutional affiliations.



Copyright: © 2022 by the authors. Licensee MDPI, Basel, Switzerland. This article is an open access article distributed under the terms and conditions of the Creative Commons Attribution (CC BY) license (<https://creativecommons.org/licenses/by/4.0/>).

Abstract: Here, we present an innovative and creative sustainable technique for the fabrication of titania (TiO₂) using *Acorus calamus* (*A. calamus*) leaf extract as a new biogenic source, as well as a capping and reducing agent. The optical, structural, morphological, surface, and thermal characteristics of biosynthesized nanoparticles were investigated using UV, FTIR, SEM, DLS, BET, and TGA-DSC analysis. The phase formation and presence of nanocrystalline TiO₂ were revealed by the XRD pattern. FTIR analysis revealed conjugation, as well as the presence of Ti–O and O–H vibrational bands. The nanoparticles were noticed to be globular, with an average size of 15–40 nm, according to the morphological analysis, and the impact of size quantification was also investigated using DLS. The photocatalytic activity of bare, commercial P-25 and biosynthesized TiO₂ (G-TiO₂) nanoparticles in aqueous solution of rhodamine B (RhB) dye was investigated under visible light irradiation at different time intervals. The biosynthesized TiO₂ nanoparticles exhibited strong photocatalytic activity, degrading 96.59% of the RhB dye. Different kinetic representations were utilized to analyze equilibrium details. The pseudo-first-order reaction was best suited with equilibrium rate constant (K₁) and regression coefficients (R²) values 3.72 × 10^{−4} and 0.99, respectively. The antimicrobial efficacy of the prepared nanoparticles was investigated using the disc diffusion technique. Further, biosynthesized TiO₂ showed excellent antimicrobial activity against the selected gram-positive staining (*B. subtilis*, *S. aureus*) over gram-negative (*P. aeruginosa*, *E. coli*) pathogenic bacteria in comparison to bare TiO₂.

Keywords: biosynthesis; nanoparticles; dye degradation; rhodamine B; antimicrobial activity

1. Introduction

The recent progress in nanotechnology has caught the interest of scientists across a wide range of disciplines because it could be used for the detection, diagnosis, and purification of environmental contaminants [1]. The study of nanostructures requires a better understanding of the crystal form with a suitable structure that can be achieved through a new design and simple synthesis methods [2]. Biogenesis has grown rapidly in modern

nanotechnology over the last few decades. The eco-friendly synthesis of nanoparticles has seen tremendous progress in nanoscience and its application in a wide range of fields such as the catalysis, antimicrobial [3], anticancer [4], target-specific drug delivery [5], and agriculture [6] fields. Recently, several biosynthesis methods have been suggested in order to develop potential sustainable synthesis techniques to reduce the use of hazardous materials for nanomaterials [7]. There has been a spike in interest in fabricating nanomaterials using sustainable green technologies in recent years. The structure of inorganic nanoparticles, showing significantly novel and enhanced features due to their nanoscale sizes, have gained great interest [8,9]. Textile dyes discharged into nearby water during the dyeing process have become a serious health threat for individuals and their surroundings. The degradation of dye is almost crucial for wastewater due to its toxicity. As a result, a method for using biosynthesized nanoparticles from a wide range of biomedical applications has been reported, with plant material being the most suitable approach. Since plant material is easily accessible, it not only makes the process eco-friendlier, but also more cost-effective.

Titanium dioxide nanoparticles can be synthesized using several techniques, such as the template [5,10], sol-gel [11], hydrothermal [12], thermal hydrolysis [13], electrochemical anodic oxidation [10], flame synthesis [14,15], and photochemical reduction methods [16,17]. The most common precursors used to synthesize TiO₂ nanoparticles were titanium (IV) alkoxide, titanium tetra isopropoxide (TTIP), titanium butoxide, and titanium tetrachloride (TiCl₄). Titanium tetrachloride is the most toxic and corrosive of these precursors, while titanium (IV) alkoxide is both costly and soluble in organic solvents. The green route is the more suitable option for nanoparticle synthesis, since it is more sustainable and eco-friendlier, while physical and chemical methods for synthesis are also possible [18]. Several researchers successfully synthesized TiO₂ using eco-friendly plant materials such as leaves [3], roots [4], and fruits [19] for dye degradation. A range of phytochemicals and bioactive compounds have been found in common aqueous extracts from various medicinal plants that work as non-toxic capping and reducing agents, and shape and size control agents for synthesized nanoparticles [7,20]. As a result, the presence of various stabilizing agents is advantageous for controlling particle size and growth.

TiO₂ is well known among metal oxides as a multifunctional material that plays an essential role in a variety of applications due to its good physical stability and non-toxicity [21]. Anatase, rutile, and brookite are the three main polymorphs of TiO₂ nanostructure. Anatase TiO₂ has a high catalytic activity due to its large surface area, high molecular oxygen adsorption capacity, and low rate of electron-hole pair recombination [22]. Anatase TiO₂ nanocatalysts with wide-bandgap semiconductors have been studied extensively due to their excellent photocatalytic activity under UV irradiation [18]. Sharma et al. reported that cerium oxide (CeO₂) nanoparticles were successfully synthesized via *A. indica* leaf extract and used as a nanocatalyst for the photodegradation of RhB dye. Similarly, TiO₂ and CeO₂ nanoparticles have a wide bandgap, are mostly non-toxic, and have high stability, making them an alternative material for photocatalytic applications [23]. The co-precipitation method was used to fabricate a nanocomposite and investigate photocatalytic performance of BPB dye in an aqueous solution under solar irradiation using TiO₂-laced nanocomposite with activated carbon and clinoptilolite. The degradation efficiencies of BPB dye with TiO₂-doped catalyst found that the highest photocatalytic performance was about 70 to 90% as compared to TiO₂ using 4 g of catalyst dosage [24].

A. calamus is a traditionally well-known medicinal plant used in the treatment of many diseases. *A. calamus* was originally classified as a member of the Araceae family but is now designated as belonging to the Acoraceae family [25]. The plant grows in northern temperate and subtropical regions of Asia, as well as North America, Europe, and northern Jammu and Kashmir of India [26]. A semiaquatic herb with creeping rhizomes, it has a wide range of pharmacological characteristics, including antibacterial, insecticidal, and anti-ulcerative effects. The major bioactive chemicals contained in *A. calamus* are flavonoid, monoterpene, quinone, sesquiterpene, and phenylpropanoid [27]. Researchers have intro-

duced a wide range of antimicrobial agents that are multidrug-resistant and can treat a wide range of microbial diseases [28,29]. The use of metal and metal-based nanoparticles as a novel antibacterial drug formulation is a cutting-edge and unique approach to drug development. The motive of this study is to explore the optical, structural, and morphological features of biosynthesized TiO₂ nanoparticles using *A. calamus* leaf extract in a green method. Additionally, biosynthesized nanoparticles were utilized to investigate photocatalytic dye degradation as well as antibacterial properties, and to compare them with the bare TiO₂ and commercial P-25 nanoparticles. To our knowledge, this is the first work to use a precipitation approach with *A. calamus* leaf extract as a stabilizing agent to synthesize TiO₂ nanoparticles, and no findings on photocatalytic or antibacterial activity have been reported.

2. Results and Discussion

2.1. Optical Properties

The UV-visible light at wavelengths ranging from 200 to 800 nm was used to evaluate the light absorption characteristics of TiO₂ nanoparticles. Figure 1 depicts the UV-visible spectra of TiO₂ and *A. calamus* leaf extract in an aqueous solution at room temperature. It was observed that the absorption maxima (λ_{\max}) for bare and biosynthesized TiO₂ (G-TiO₂) were found to be 341 and 355 nm, respectively, which is a preliminary indication of TiO₂ material presence (Figure 1a) [9]. Our goal is to determine photocatalytic activity; hence the bandgap of the material is important. As a result, we used the UV-visible spectrum to evaluate the optical nature, bandgap energy absorption edge, and other properties of TiO₂ nanoparticles calcined at 600 °C. The optical bandgap (E_g) of the biosynthesized samples was determined using the Tauc plot, $h\nu$ vs $(\alpha h\nu)^2$, as indicated in Figure 1b using the following Equation (1):

$$(\alpha \cdot h\nu)^{\frac{1}{n}} = k(h\nu - E_g) \quad (1)$$

where k is a constant, $h\nu$ is the photon energy, E_g the bandgap energy and the absorption coefficient (α). The n factor equals 1/2 or 2 for the indirect and the direct band gaps, respectively, depending on the nature of the electric transition. The absorption peak obtained at 341 nm is assigned to a characteristic peak of monodispersed TiO₂ nanoparticles [18]. The bandgap energy of biosynthesized TiO₂ nanoparticles was calculated to be 3.20 eV. This value is similar to bulk titanium dioxide, i.e., $E_g = 3.22$ eV [30]. These results further confirmed the formation of TiO₂ nanoparticles.

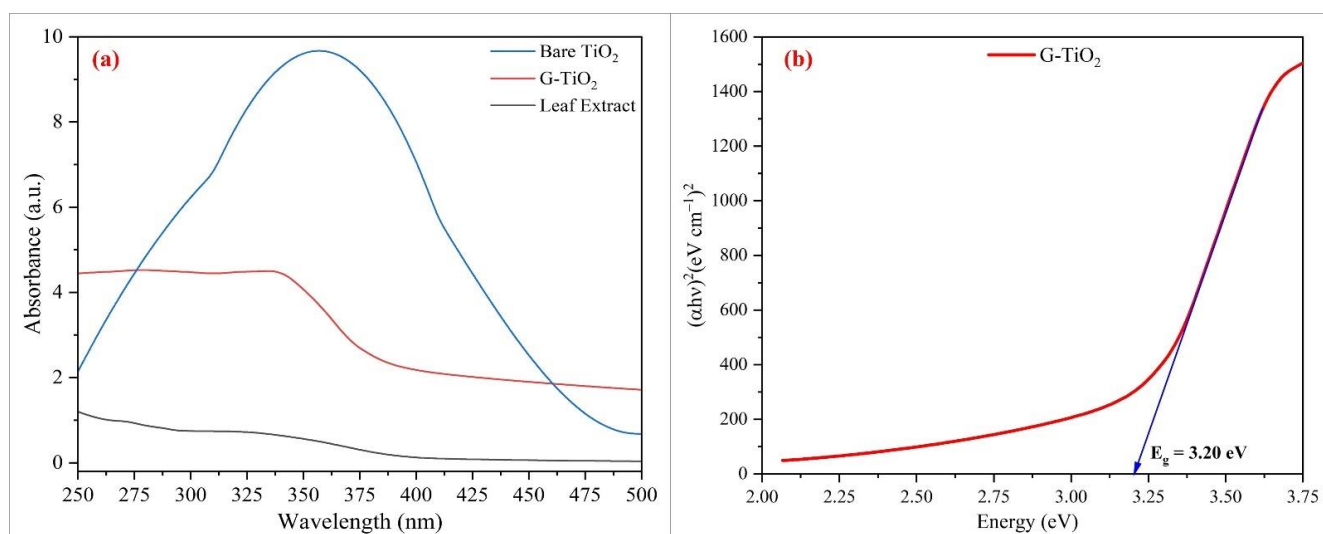


Figure 1. UV-visible spectra and tauc plot: (a) spectra of leaf extract, bare and biosynthesized TiO₂ nanoparticles; (b) tauc plot of biosynthesized TiO₂ nanoparticles.

2.2. Functional Groups Analysis

The different functional groups on the surface of leaf extract, bare TiO_2 , and biosynthesized TiO_2 nanoparticles were determined using the FTIR spectrum (Figure 2). The absorption peaks of biosynthesized nanoparticles were found to be below 1200 cm^{-1} . In the spectrum for leaf extract, the major stretching frequencies were observed at 3260 , 2096 , 1583 , 1400 , 1305 , 1066 , and 756 cm^{-1} . Hydroxyl groups were attributed to the band 3260 cm^{-1} , whereas carbonyl stretching vibrations and asymmetric carboxylate stretching were assigned to the bands 2096 cm^{-1} and 1583 cm^{-1} , respectively [12,19,31]. The symmetrical twisting vibration of the $-\text{COO}$ group caused the band 1400 cm^{-1} , confirming the presence of a carboxylic group in the extract. The bending oscillation of the C-H group in the aldehydes was disclosed by the band at 1305 cm^{-1} , whereas the C-O pulling oscillations of the ether and tertiary alcohols were shown by the bands at 1066 and 756 cm^{-1} , respectively [32]. The non-appearance of these unique crests in the spectral band of synthesized nanoparticles by leaf extract could be attributed to the enhanced precision of synthesized nanoparticles in anatase crystal form after $600\text{ }^\circ\text{C}$ calcination. The bare TiO_2 nanoparticles spectra were also used to provide comparative studies with the biosynthesized nanoparticles. The bare TiO_2 spectra contain various wide vibrational bands and functional groups. The band appeared in the range 3339 cm^{-1} with the characteristics of $-\text{OH}$ stretching and the band at 1627 cm^{-1} with the characteristics of $-\text{OH}$ bending vibration of water molecules absorbed on the surface of bare TiO_2 . Ti-O-Ti vibrations were responsible for the distinctive indication for TiO_2 nanoparticles recorded in the FTIR spectra below 1000 cm^{-1} [33]. FTIR spectroscopy was also used to provide comparative spectra of TiO_2 with *A. calamus* leaf extract (Figure 2). It is possible to show that phytochemicals contained in *A. calamus* leaf extract might be for the depletion of metallic ions (Ti^{+4}) in the commencing material, which is effective in the biosynthesis G-TiO_2 nanoparticles, using leaf extracts from selected medicinal plants [3].

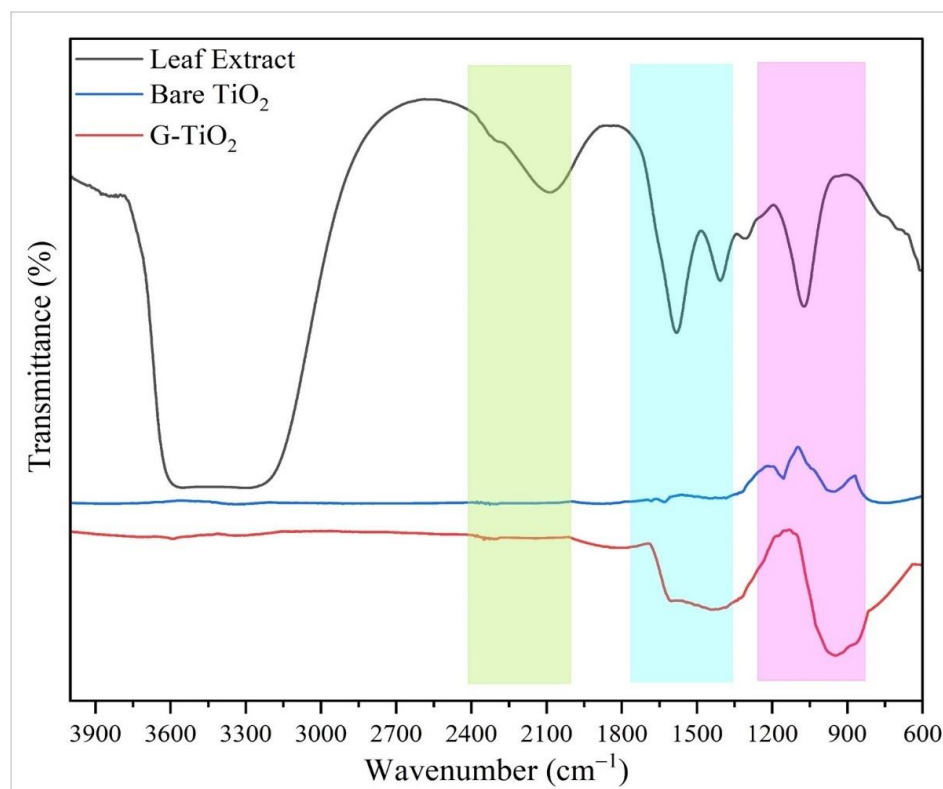


Figure 2. FTIR spectra of leaf extract, bare and biosynthesized TiO_2 nanoparticles.

2.3. Crystallographic Structure

Figure 3 shows the XRD pattern of biosynthesized and bare TiO₂ nanoparticles. The spectra show the development of anatase-phase titania with diffraction angles (2θ) of 25.3° (110), 37.8° (011), 48.0° (111), 54.0° (121), 62.8° (310), 69.0° (031), 70.2° (112), and 75.1° (022). Our findings are very similar to those of the standard JCPDS File No (21-272). From the XRD spectra, a prominent peak at 25.3° and 48.0° is solely related with the TiO₂ anatase (110) crystallographic plane without the presence of any impurities. Further, the XRD spectra of bare TiO₂ were also provided for the comparison with the biosynthesized nanoparticles. The broad peaks in the spectra indicate that the particles are relatively small. The peak intensities of biosynthesized TiO₂ are higher than bare TiO₂, which could be attributed to slight variations in titania grain size. The XRD sample of bare TiO₂ showed a dominant peak at (2θ) of 27.3° and 41.8° which proved the (110) crystallographic plane of both the anatase and (111) rutile form of TiO₂ NPs, respectively. Our XRD results coincide with the work reported on the synthesis of catalyst particles derived by the sol-gel approaches. Comparatively, the broader diffraction peaks corresponding to the bare TiO₂ sample was attributed to the presence of the smaller crystallite size. The stoichiometry of the final matter is highly dependent on the restricted pressure used during the production [19]. As a result, the stoichiometries of biosynthesized TiO₂ nanoparticles could be very diverse. The crystallite size and peak broadening profile of the synthesized nanoparticles were estimated using the Debye Scherrer formula ($D = 0.9\lambda/\beta \cos \theta$) at a 2θ value of 25.3°. The size of biosynthesized nanoparticles was determined to be around 38.6 nm. Apparently, the reported nanocrystallite sizes clearly revealed that biosynthesized nanoparticles have the smallest size, which is consistent with the SEM results. The presence of strong peaks supported the crystallinity of TiO₂ nanoparticles in the anatase form, whereas the absence of spectra represented alternative TiO₂ crystallite forms [32].

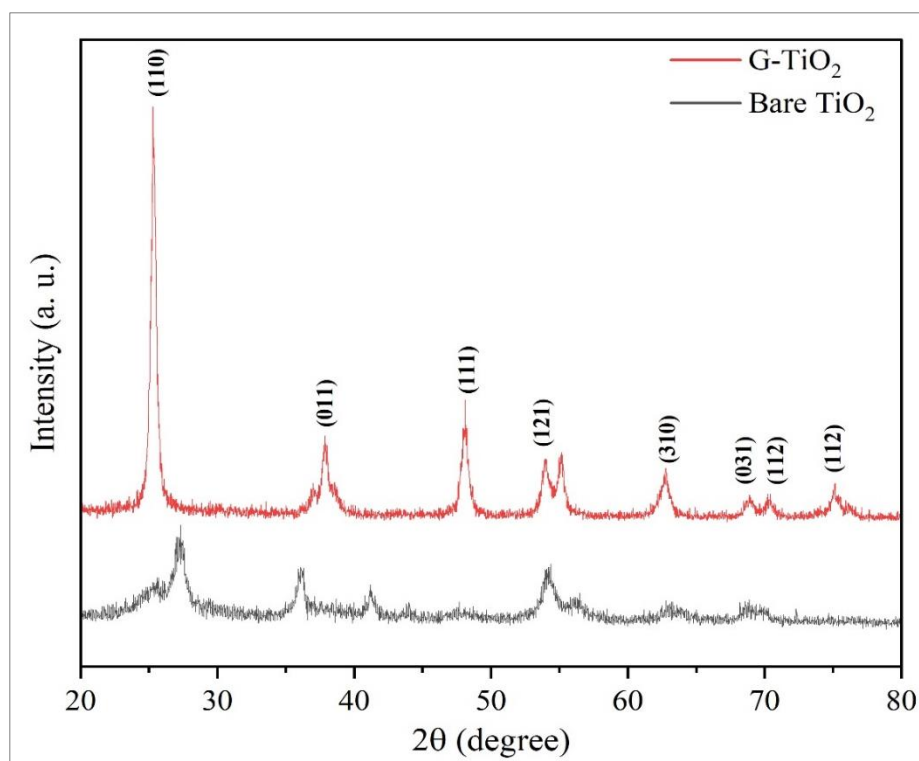


Figure 3. XRD spectra of biosynthesized and bare TiO₂ nanoparticles.

2.4. Morphology Analysis

The morphology, such as shape, size, and surface characteristics, were investigated using scanning electronic microscopy. The SEM micrographs of biosynthesized with

A. calamus plant leaf extract and bare TiO₂ nanoparticles is shown in Figure 4. The fabricated facile nanoparticles are uniformly dispersed, spherical, and interconnected, as shown by SEM micrographs (Figure 4a). The average build of the biosynthesized TiO₂ nanoparticles was determined using SEM micrographs, and it was found to be in the 11–30 nm range. Figure 4b depicts high magnification pictures of as-prepared TiO₂ nano powder samples deposited on carbon stripes. The nanoparticles are densely aggregated in the form of large clusters around the examining area, but the approximate average size of the nanoparticles is 108 nm, and they are semi-spherical in shape. The particle size of biosynthesized TiO₂ is slightly smaller than the rest of the bare TiO₂ that was generated at low temperature and high concentration, as can be seen in the SEM micrographs. According to Sankar et al., interconnected nanoparticles are mostly used for electrochemical and biological applications [34]. Furthermore, the synthesized nanoparticles sizes might be comparable to the other previously reported Degussa P25 Mixed-Phase TiO₂ nano powder [2,35]. However, there is a slight difference in particle sizes between the two samples, which could be attributable to the synthesis conditions.

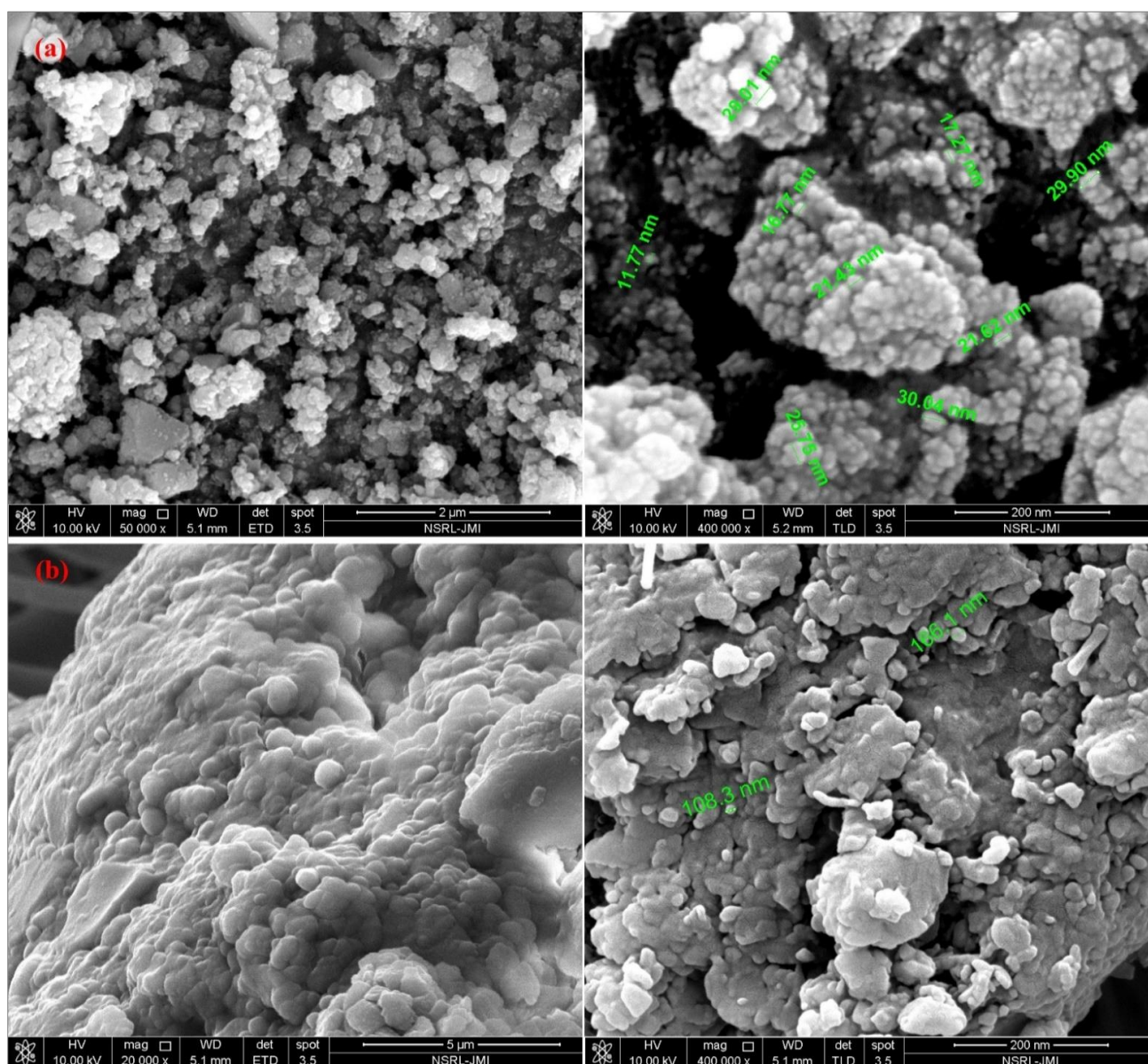


Figure 4. SEM micrographs of (a) biosynthesized and (b) bare TiO₂ nanoparticles.

2.5. DLS Analysis

The hydrodynamic diameter of biosynthesized and bare TiO₂ nanoparticles was precisely measured using particle size analysis. The mean particle size of biosynthesized and bare TiO₂ nanoparticles was estimated to be 37.8 and 58.8 nm, respectively (Figure 5a). The particle size distribution curve for biosynthesized TiO₂ exhibited an intensity of 8.83%, while bare TiO₂ showed 7.19%, which indicates some agglomerations in the solvent (Figure 4a). However, chemically synthesized nanoparticles were agglomerated up to 2.3 μm [4,18]. The zeta potential is used to discover the charge and firmness of a solid particle in an aqueous suspension. It is based on dynamic light scattering (DLS). In our recent investigation, we found a significant positive zeta potential of biosynthesized nanoparticles approximately 4.65 mV, compared to 5.81 mV for bare TiO₂ (Figure 5b). The high absolute value of zeta potential indicates that the nanoparticles have a high electrical charge on their surface that shows stability of nanoparticles.

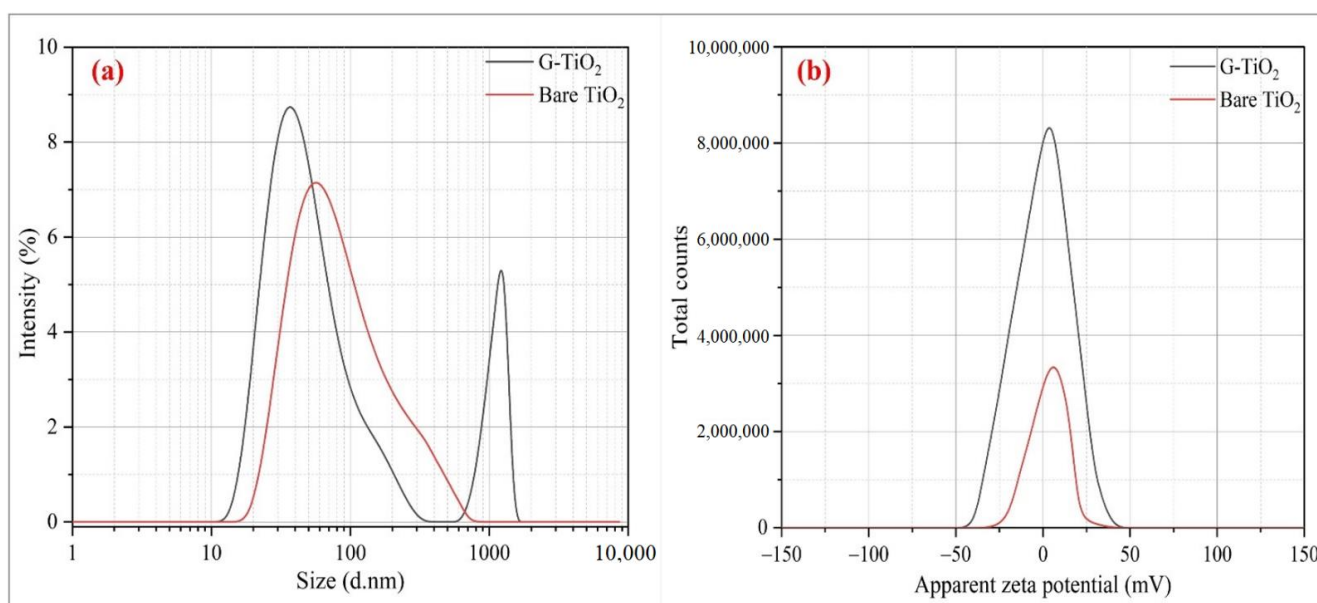


Figure 5. DLS analysis (a) particle size distribution (b) apparent zeta potential of biosynthesized and bare TiO₂ nanoparticles.

2.6. BET Analysis

For exploring the facet behavior of biosynthesized TiO₂ nanoparticles, adsorption–desorption spectra were documented using Brunauer–Emmett–Teller (BET) analysis, as shown in Figure 6. The adsorption–desorption isotherm was a classic type IV with an H4 hysteresis curve and mesoporous phases, as per IUPAC nomenclature [36]. This indicates uncontrolled multilayer formation, since the lateral contact between adsorbed molecules is stronger than on adsorbate and adsorbent surfaces. The porous character of the material is confirmed by the wide and broad hysteresis loop with a delay in the condensation–evaporation process. The particular surface region of synthesized TiO₂ nanoparticles was evaluated from isotherms using BET analysis and was found to be 7.04 m² g^{−1}. The Barret–Joyner–Halenda (BJH) plot demonstrated the calculated average pore size distribution of nanoparticles from adsorption sites. Furthermore, the BJH model, which was used to calculate the average pore diameter and volume of biosynthesized TiO₂ nanoparticles samples, showed values of 4.92 nm and 5.701 cm³ g^{−1}, respectively. The increased surface area provides additional binding sites, enhancing the sorption capacity of the synthesized material. Previous research also revealed a correlation between increased pore volume and increased surface area [32,37].

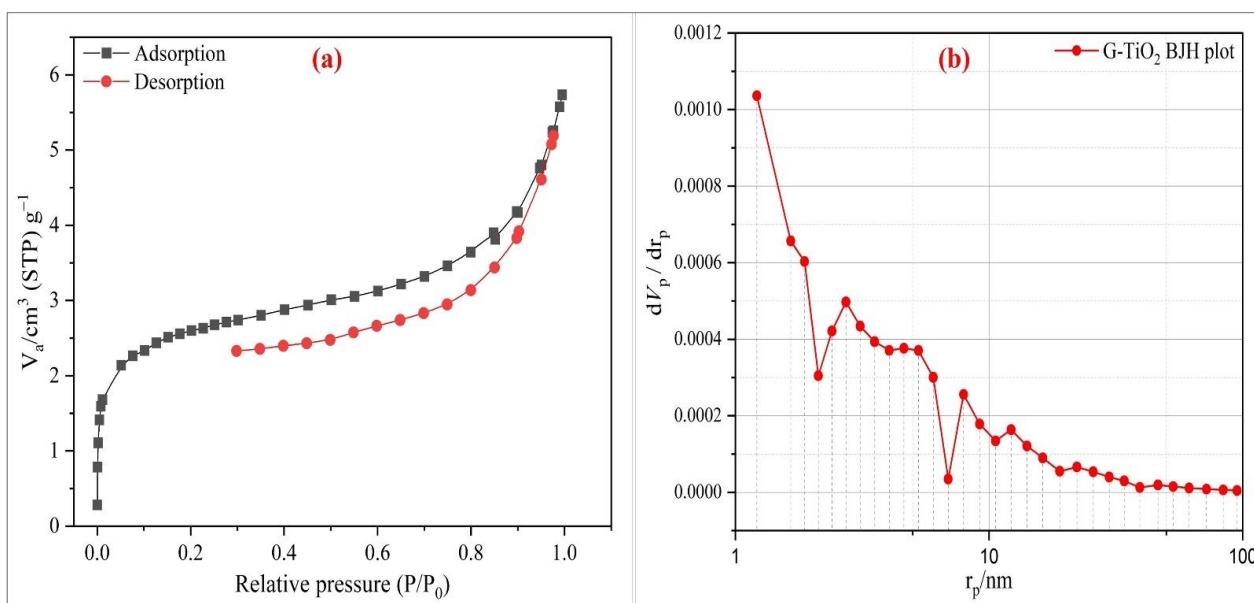


Figure 6. BET analysis. (a) Adsorption-desorption spectra; (b) BJH pore size distribution plots of biosynthesized TiO_2 nanoparticles.

2.7. Thermal Properties

The thermal characteristics of biosynthesized TiO_2 nanoparticles were investigated employing thermogravimetric analysis. The thermograms of manufactured nanoparticles heated from 25°C to 1000°C using differential scanning calorimetry (DSC) and thermogravimetry (TGA) are plotted (Figure 7). TGA experienced two significant weight loss events. Below 200°C , removing physically and chemically entrapped water molecules and aqueous ammonia from the titania gel resulted in a weight loss of around 12%. Pyrolysis and carbonization of biomass resulted in a weight loss of around 33% at temperatures ranging from 200 to 800°C [5], which is associated to the transition of titania from the amorphous to the anatase phase (i.e., the combustion of TiOH to form TiO_2 nanoparticles) [38].

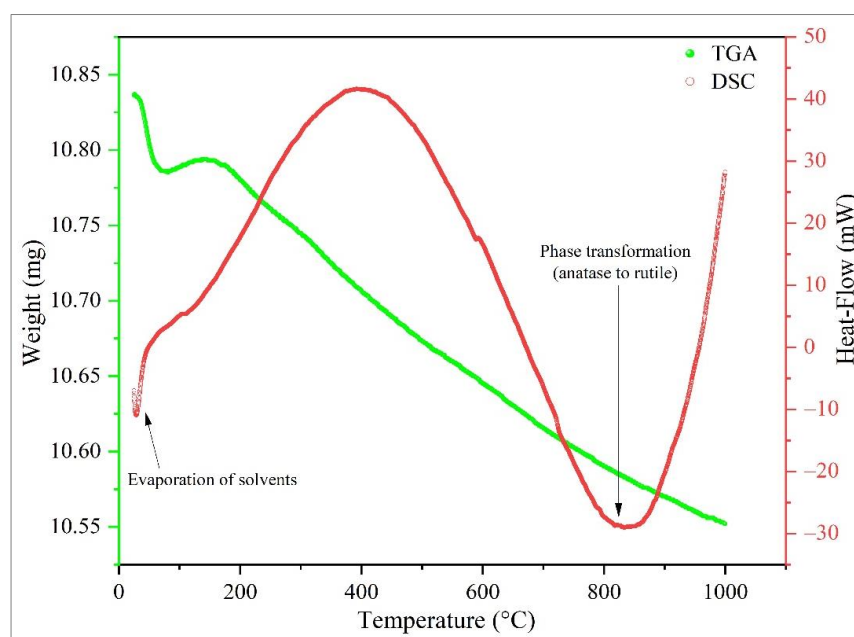


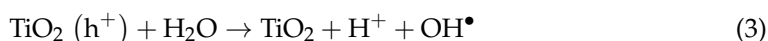
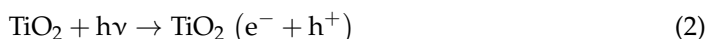
Figure 7. TGA and DSC thermograms of biosynthesized TiO_2 nanoparticles.

On the DSC thermogram, similar peaks can be observed, indicating two phases. It has two endothermic peaks, one at around 100 °C and the other at approximately 800 °C. At 400 °C, the vaporization of carbonized residues on the surface of biosynthesized nanoparticles indicated a high exothermic peak. There have been other investigations that have shown similar outcomes to this one [39]. There was no significant weight loss from 800 °C to 1000 °C, thus 600 °C was preferred as the calcination temperature for this study based on thermal analysis.

2.8. Photocatalytic Activity

Under visible light, the catalytic activity of biosynthesized, bare, and commercial P-25 TiO₂ nanoparticles were demonstrated using RhB dye, and degradation was initially determined by color change. The dye exhibited a unique absorption spectrum in visible light at 554 nm, where absorption was maximum. The dye concentration in the solution was assessed and recorded using this peak. The photocatalytic degradation of RhB dye is time-dependent and increases with increasing irradiation time. As can be observed from the reduction in absorbance, the addition of the biosynthesized, bare and P-25 TiO₂ nanocatalyst developed in a straight rise in the degree of deterioration with passage of time (Figure 8a–c). According to this study, when the irradiation time was extended, the percentage of dye degradation improved and attained a maximum (96.59%) after 120 min of irradiation time. The results reveal that biosynthesized and P-25 TiO₂ nanoparticles have high photocatalytic activity against RhB dye in aqueous solution. The degradation rate of RhB dye was found to be greater in the case of biosynthesized TiO₂ (96.59%) after 120 min of irradiation, followed by P-25 commercial (78.90%). In the instance of biosynthesized TiO₂, the degradation rate of RhB was found to be greatest after 120 min of irradiation (Figure 8d). At the same irradiation period and dosage, higher degradation efficiency is attained with TiO₂ particles loading, as shown in Figure 8. When exposed to visible light, photo-generated charge carriers stimulated reactions on the surface of photocatalysts distributed in dye solution. As a result of the formation of electron-hole pairs, any pollutant deposited on the photocatalyst surface will be reduced or oxidized. Based on the above discussion, the biosynthesized TiO₂ nanoparticles with dominant exposed (110) and (111) facets exhibited higher photocatalytic activity, compared with that of P25-TiO₂ without an exposed specific surface [35,40].

The photo-induced chemical transformation reaction occurs on the catalyst surface in a standard photocatalytic degradation process. The production of electron-hole pairs ($e^- + h^+$) in the catalyst regulates the basic mechanism of the photocatalytic reaction, which is followed by the generation of free radicals and their transport to the target, i.e., the interaction with target chemical species such as dyes [16,24,36]. Biosynthesized TiO₂ nanoparticles were utilized as photocatalysts in this work for the catalytic degradation of dye. The equations below depict a proposed pathway of photocatalytic dye degradation with the produced molecule (Equations (2)–(5)). When the biosynthesized nanoparticles are irradiated with light during photocatalysis, h^+ reacts with H₂O or OH⁻ to produce the first photo-excited conduction band electrons (e^-) and valence band holes (h^+). As a result, an OH[•] radical is generated, which acts as a powerful oxidizing agent and degrades the RhB during the reaction, as shown below [10,36,41].



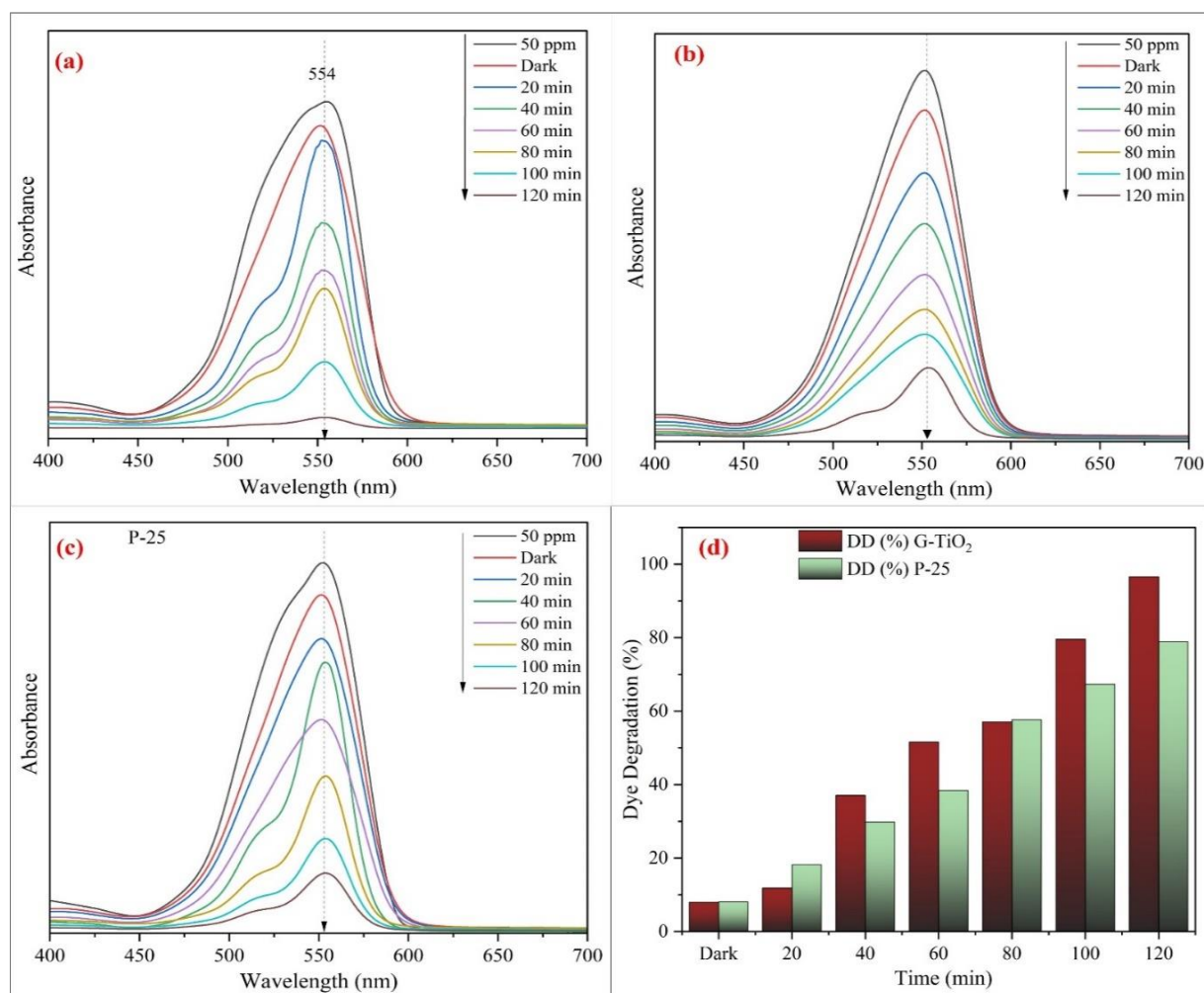


Figure 8. UV-visible absorbance graph to evaluate RhB dye degradation with (a) biosynthesized TiO₂; (b) bare TiO₂; (c) commercial P-25 nanoparticles; (d) degree of degradation.

The generation of electrons and holes in the presence of UV-visible light was the basis of photocatalysis for wastewater treatment. This electron-and-hole photogeneration generates free radicals, which are highly reactive species capable of breaking down dye molecules and purifying the water through chemical processes. The dye has a strong deionized water absorption peak, but electrons and holes will break down the dye molecules after a photocatalytic process, resulting in a rapid decrease in signal strength. As a result, a decrease in the absorbent spectrum implies both photocatalytic activity and dye degradation. The UV-vis region of electromagnetic radiation, which corresponds to the bandgap, highlights the bandgap in the visible range. Earlier research found a similar pattern of behavior [42–44].

2.9. Kinetics Study

Table 1 shows the dye degradation kinetics calculated using the pseudo-first- and second-order kinetics models. For the pseudo-first-order reaction, a graph of $\ln(Q_e - Q_t)$ versus t was drawn (Figure 9a), and the equilibrium rate constant (K_1) was determined from the slope with a value of 72×10^{-4} and regression coefficients of 0.99, respectively. The theoretical value of equilibrium concentration of RhB dye was 91.85 mg g^{-1} for TiO₂, while the experimental value was 96.59 mg g^{-1} with a difference of 4.74 mg g^{-1} . Similarly, A graph of t/Q_t versus t was drawn for the pseudo-second order (Figure 9b), and the rate constant (K_2) was calculated from the intercept with a value of $2.46 \times 10^{-4} \text{ g mg}^{-1} \text{ min}^{-1}$,

with a regression coefficient of 0.60, respectively. The theoretical value of equilibrium concentration of RhB dye was 160.67 mg g^{-1} for TiO_2 , while the experimental value was 96.59 mg g^{-1} with a difference of 64.08 mg g^{-1} [45]. When compared to data from the pseudo-first-order and pseudo-second-order kinetics models, it is clear that the data from the pseudo-first-order model is more reliable than the data from the pseudo-second-order model, particularly in terms of the proximity of regression coefficient and the theoretical and experimental values of equilibrium concentrations. Therefore, the kinetics is determined by a pseudo-first-order reaction. The photodegradation was distributed over different intervals of time, as shown in Figure 8a, which were characterized by the respective specific apparent rate constants. The rapid decomposition of RhB dye was observed during the initial irradiation period. This is mainly due to the degradation affected by adsorption. The findings of this study are consistent with those of previous studies [37,46].

Table 1. Kinetics models of RhB dye degradation using biosynthesized TiO_2 nanoparticles.

		Pseudo First Order			
Catalyst	Dye	$Q_e \text{ (mg g}^{-1}\text{)}$		$K_1 \text{ (min}^{-1}\text{)}$	R^2
		Calculated	Experimental		
TiO_2	RhB	91.85	96.59	0.000372	0.9905
		Pseudo Second Order			
Catalyst	Dye	$Q_e \text{ (mg g}^{-1}\text{)}$		$K_2 \text{ (g mg}^{-1} \text{ min}^{-1}\text{)}$	R^2
		Calculated	Experimental		
TiO_2	RhB	160.67	96.59	0.000246	0.6001

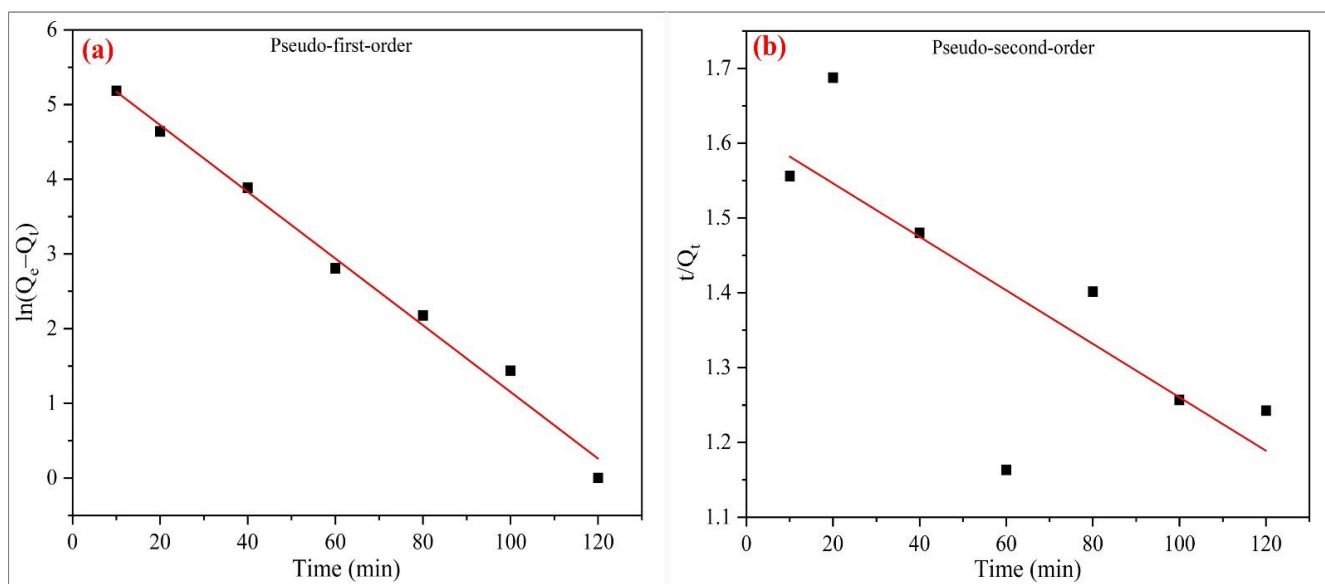


Figure 9. Plots of kinetic models showing degradation of RhB dye; (a) pseudo-first-order, (b) pseudo-second-order.

2.10. Antimicrobial Assessment

In vitro analysis was used to assess the antibacterial efficacy of biosynthesized and bare TiO_2 nanoparticles against gram-negative (*P. aeruginosa*, *E. coli*) and gram-positive (*B. subtilis*, *S. aureus*) human pathogens. The different concentrations of nanoparticles taken for analysis are given in Table 2. The leaf extract of *A. calamus* showed no zone of inhibition against pathogenic bacteria in both conditions, while the solution of 10 and $20 \mu\text{g mL}^{-1}$ of biosynthesized and bare TiO_2 dosage showed a clear zone of inhibition

which is an effective dosage for antimicrobial activity in both pathogens (gram-negative and gram-positive). Further, the inhibition zone with biosynthesized TiO₂ dosages (10 and 20 µg mL⁻¹) was 6 ± 0.2, 8 ± 0.3 mm, and 9 ± 0.3, 10 ± 0.2 mm in gram-negative and 12 ± 0.4, 14 ± 0.5 mm, and 10 ± 0.3, 12 ± 0.3 mm in gram-positive bacteria, respectively (Figure 10a–d). Additionally, the antimicrobial activity tested for bare TiO₂ has shown a high degree of susceptibility against both bacteria. The biosynthesized nanoparticle shows a high degree of bactericidal nature with the increased dosage concentration in compared to the bare TiO₂ nanoparticle. It is observed an increase in the zone of inhibition with increasing concentration (10 and 20 µg mL⁻¹) of bare TiO₂ nanoparticles. The zone of inhibition with bare TiO₂ dosage (10 and 20 µg mL⁻¹) was 4 ± 0.6, 6 ± 0.3 mm, and 6 ± 0.4, 8 ± 0.6 in gram-negative and 9 ± 0.6, 8 ± 0.4 mm, and 10 ± 0.2, 11 ± 0.6 mm in gram-positive bacteria, respectively (Figure 10e–h). From the figure, it has been also observed that an increasing dosage concentration of nanoparticles improves antibacterial activity, and good performance was obtained against gram-positive (*B. subtilis* and *S. aureus*) bacteria compared to gram-negative bacteria (*P. aeruginosa* and *E. coli*).

Table 2. Disc diffusion analysis of biosynthesized TiO₂ nanoparticles: (A) control (B) leaf extract (C) 10 µg mL⁻¹ and (D) 20 µg mL⁻¹ treatments.

Bacterial Strains	Treatment	Control (A)	Inhibition Zone (mm)		
			(B) Leaf Extract	(C) 10 µg mL ⁻¹	(D) 20 µg mL ⁻¹
<i>Escherichia coli</i> (ATCC 25922)	Biosynthesized TiO ₂	0	0	9 ± 0.3	10 ± 0.2
<i>Pseudomonas aeruginosa</i> (ATCC 27853)		0	0	6 ± 0.2	8 ± 0.3
<i>Bacillus subtilis</i> (ATCC 6633)		0	0	12 ± 0.4	14 ± 0.5
<i>Staphylococcus aureus</i> (ATCC 25923)		0	0	10 ± 0.3	12 ± 0.3
<i>Escherichia coli</i> (ATCC 25922)	Bare TiO ₂	0	0	4 ± 0.6	6 ± 0.3
<i>Pseudomonas aeruginosa</i> (ATCC 27853)		0	0	6 ± 0.4	8 ± 0.6
<i>Bacillus subtilis</i> (ATCC 6633)		0	0	9 ± 0.6	8 ± 0.4
<i>Staphylococcus aureus</i> (ATCC 25923)		0	0	10 ± 0.2	11 ± 0.6

The greater performance of TiO₂ nanoparticles upon both pathogens might be due to the stronger interaction among metal ion surfaces with microbial factors [31,47]. The biosynthesized TiO₂ nanoparticles are effective antibacterial agents because they dissolve the outer cell of bacteria, which is primarily responsible for bacterial death. TiO₂ nanoparticles diffuse the outside cell of bacteria because of the existence of a hydroxyl group. The released ions may interact with the bacterial cell wall, facilitating in bacterial cell breakdown and development of antibacterial properties. The released ions are loosely bound with TiO₂ on the matrix surface to continue a thermodynamically more beneficial interaction with the bacterial cells, resulting in enhanced antimicrobial activity. When compared to previous studies on antimicrobial activity, biosynthesized nanoparticles were used in this work and found to perform better than previously reported studies [48,49].

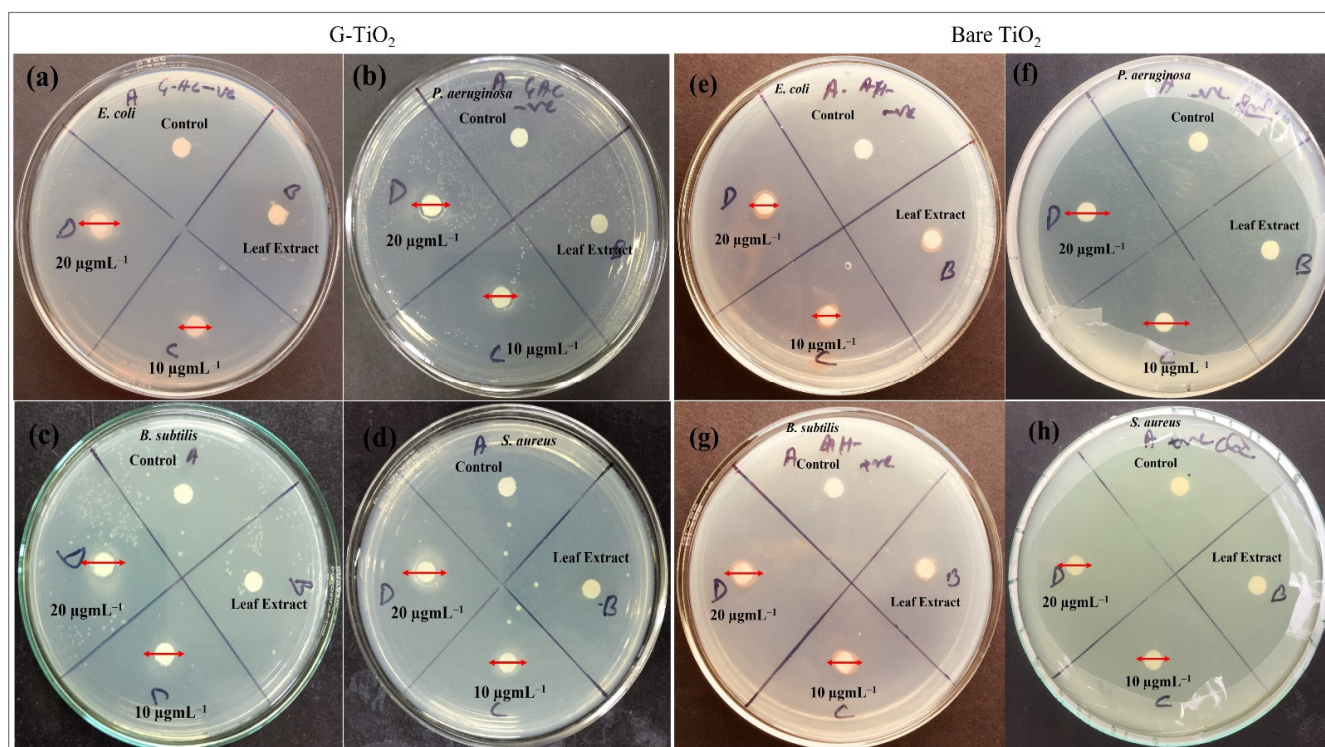


Figure 10. Assessment of antimicrobial efficiency of biosynthesized (G-TiO₂) and bare TiO₂ nanoparticles against Gram-negative (a,b,e,f) and Gram-positive bacteria (c,d,g,h).

3. Experimental Section

3.1. Materials

The plant of *A. calamus* was collected by one of the authors from the local area of Rehtal, Rajouri (33°24'47.5596'' N latitude and 74°20'9.3588'' E longitude), Jammu and Kashmir, India. Titanium (IV) isopropoxide (TTIP, C₁₂H₂₈O₄Ti) [97% liquid analytical grade], commercial P-25, and Whatman filter paper, Grade-1 were procured from Sigma-Aldrich Chemicals Pvt Ltd., Mumbai, India. Rhodamine B dye (RhB), Isopropanol, and aqueous ammonia were obtained from Thermo Fisher Scientific Pvt. Ltd., New Delhi, India. All of the compounds used in the tests were analytical grade and had not been refined any further. All suspensions and solutions were prepared with deionized water. Before using, all glassware was washed in weak nitric acid and dried in the oven.

3.2. Preparation of Plant Extract

The healthy plant leaves of *A. calamus* were cleaned twice with deionized water and dried with a blotting paper towel. 20 g of finely chopped healthy leaves were mixed with 100 mL of sterile deionized water in a 250 mL Erlenmeyer flask, and the leaf extract was made by heating at 80 °C for 60 min using the Soxhlet extraction procedure. The extracted solution was then filtered with Whatman filter paper, Grade-1 to remove particle debris, and the filtrates were kept at 4 °C for future use.

3.3. Green Synthesis of TiO₂ Nanoparticles

To synthesize TiO₂ nanoparticles in a sustainable manner, *A. calamus* leaf extract was used as a reducing and capping agent, and titanium (IV) isopropoxide (TTIP) was used as a precursor. To begin the synthesis, 2.5 mL of TTIP (0.05 M) was dissolved in 100 mL of deionized water while stirring constantly until a transparent solution was obtained. The blend was then prepared with 20 mL of leaf extract before being treated with aqueous ammonia at room temperature with constant stirring until the pH reached 7. The synthesized product was washed several times with deionized water and filtered using

Whatman filter paper before being oven-dried overnight at 50 °C. The dry precipitate was pulverized with an agate mortar pestle and calcined in a temperature-controlled muffle furnace for 3 h at 600 °C. Chemical sol-gel techniques were also used to synthesize bare TiO₂ nanoparticles [50]. Finally, the XRD technique was used to assess the phase purity and crystallinity of plant-mediated TiO₂ nanoparticles.

3.4. Instrumentations and Characterizations

The absorption spectrum between 200–800 nm was investigated using an ultraviolet-visible (UV-Vis) absorbance spectrophotometer (Hitachi model-U3900, Tokyo, Japan). The absorption band of biosynthesized nanoparticles was studied using Fourier transform infrared spectroscopy (FTIR, Model—Bruker Tensor 37, Billerica, MA, USA) at room temperature in transmission mode (cm⁻¹) with the KBr pellet (1:20) approach. The structural study of synthesized TiO₂ was observed using a diffractometer (XRD, Rigaku Ultima IV, Tokyo, Japan) from 20 to 80° utilizing monochromatic Cu K radiation ($\lambda = 1.54 \text{ \AA}$) with an accelerating voltage of 40 kV and 40 mA at a scanning rate of 10° min⁻¹. A field emission scanning electron microscopy (FESEM, Model No. SIGMA VP, Zeiss, Germany) with a 10 kV accelerating voltage was used to analyze the surface morphology. Furthermore, the affirmation of the particle size distribution profile and zeta potential was also performed by Dynamic Light Scattering (DLS, Model No. Malvern, Zetasizer Nano ZS, Malvern, UK). Thermal decomposition and more suitable sintering temperature of synthesized nanoparticles were measured using thermogravimetric and differential thermal analysis (TGA-Q600 from TA INSTRUMENT, New Castle, DE, USA). The surface behavior (surface area and pore volume) of the biosynthesized TiO₂ was evaluated at 150 °C for 12 h using a Bruner–Emmett–Teller (BET, Quantachrome Instruments, NOVA 2200E, Boynton Beach, FL, USA).

3.5. Photocatalytic Activity

The photocatalytic efficiency of biosynthesized, commercial P-25 and bare TiO₂ nanoparticles was investigated using the degradation of RhB dye. To achieve adsorption-desorption equilibrium on the surface of catalysts, 25 mg of TiO₂ were added to 50 mL of 50 mg L⁻¹ reactive RhB dye solution, and the interruption was established in the dark with gradual stirring for 30 min. No significant changes in the reaction were observed under the different experimental conditions in the dark, so the irradiation time was optimized to 30 min. The mixture was then exposed to visible light (visible LED lamp, Philips energy saver 40 W, New Delhi, India) [51]. According to manufacturer data, the luminous flux of the LED light bulb was 4000 lumens (lm). A luxometer (LT LUTRON, Taipei, Taiwan) was utilized to measure the intensity of the visible light reaching the surface of catalysts in the reactor, which was 40,000 lux. The intensity of the lamp at 555 nm was 5.85 mW/cm² [52]. At precise regular time intervals, 2.0 mL aliquots were withdrawn for the measurement of percent degradation (Equation (6)) at 554 nm.

$$\text{Photodegradation efficiency (\%)} = \frac{C_0 - C_t}{C_0} \times 100 \quad (6)$$

where C_0 is the initial concentration of dye before illumination and C_t is the concentration of dye after time t .

3.6. Kinetics Model

The removal threshold was presented as a function of time to explore the kinetics involved in the dye degradation process. The kinetics of biosynthesized TiO₂ nanoparticles was studied by removing RhB dye at different intervals. A fixed number of synthesized nanoparticles was kept in an RhB solution with constant stirring under visible light until equilibrium. At the predetermined time interval, 2.0 mL of sample was taken from the reaction flask and measured at 554 nm using a UV-spectrophotometer. The concentration

of RhB after degradation at time t (Q_t) was calculated using the following equation, which can be represented as follows:

$$Q_t = \frac{C_0 - C_t}{m} \times V \quad (7)$$

where C_0 and C_t are the RhB dye concentrations (mg g^{-1}) before and after adsorption, respectively; m (mg) is the mass of nano photocatalyst; and V (mL) is the volume of the solution.

The kinetic data were calculated using pseudo-first-order and pseudo-second-order model equations. The derived pseudo-first-order kinetic model for solution/solid systems has the following linear form [53,54]:

$$\ln(Q_e - Q_t) = \ln Q_e - (K_1)t \quad (8)$$

where Q_e and Q_t represent the amount of RhB molecules degraded by the TiO_2 at equilibrium (mg g^{-1}), respectively, at time t . K_1 is the rate constant (min^{-1}) of the first-order reaction.

The pseudo-second-order kinetic model is based on a rate-determination stage in adsorption photoluminescence. The linear representation of the resulting pseudo-second-order kinetic model is as follows [45,55]:

$$\frac{1}{Q_t} = \frac{1}{K_2 Q_e^2} + \frac{t}{Q_e} \quad (9)$$

where t represents time and K_2 is the pseudo-second-order rate constant of the reaction.

3.7. In Vitro Susceptibility Test

3.7.1. Bacterial Strain Preparation

Pseudomonas aeruginosa (*P. aeruginosa* ATCC 27853), *Escherichia coli* (*E. coli*, ATCC 25922), and *Bacillus subtilis* (*B. subtilis*, ATCC 6633), *Staphylococcus aureus* (*S. aureus* ATCC 25923) were acquired from the HiMedia Laboratories Pvt. Ltd. Mumbai, India. All the bacterial strains were cultured in liquid medium Mueller Hinton broth (M-H Broth) (HiMedia, Mumbai, India) at 37 °C for 24 h with 200 rpm stirring.

3.7.2. Disc Diffusion Method

The antimicrobial efficacy of biosynthesis and bare TiO_2 nanoparticles was performed using the Kirby–Bauer disc diffusion susceptibility technique against gram-negative (*P. aeruginosa* and *E. coli*) and gram-positive (*B. subtilis* and *S. aureus*) human pathogens [56]. A 50 μL of bacterial culture was spread onto 25 mL Mueller–Hinton agar plates using a sterile cotton swab containing different concentrations (10, 20 g mL^{-1}) of synthesized nanoparticles obtained from a stock solution of 1000 g mL^{-1} , then added to the sterilized disc of 5 mm size. A sterile blank and leaf extract disc was also used in the antibacterial susceptibility test. The disc was incubated for 24 h at 37 °C on an agar-mediated plate. The inhibitory zone was revealed after 24 h of incubation. The results were expressed as the zone of inhibition mean diameter in mm with a standard deviation.

4. Conclusions

The sustainable biogenesis of TiO_2 nanoparticles using *A. calamus* plant leaf extract under physiological conditions such as room temperature is an uncomplicated, eco-friendly, and highly efficient technique. The XRD, DLS, and SEM results showed that the biosynthesized TiO_2 nanoparticles were globular and ranged in dimensions from 15 to 40 nanometer. FTIR reveals the existence of alcoholic groups via Ti–O vibrational bands, O–H bands, and carboxylic group C–O stretching. The dye degradation activity of the synthesized nanoparticles suggests that TiO_2 nanoparticles are more involved in RhB dye degradation than conventional hydrogen peroxide, which needs the use of a catalyst. Under visible light irradiation, the increased photocatalytic action of the biosynthesized TiO_2 nanoparticles is responsible for the degradation efficiency of 96.59% of the RhB. Furthermore, photocat-

alytic activity was influenced by particle morphology, with greater photocatalytic activities achieved when compared to commercial P-25 nanoparticles. Pseudo-first-order kinetic mechanism models were determined and best suited with a regression coefficient (R^2) value of 0.99. This degradation process is quick, efficient, and inexpensive, and it can be used to purify contaminated water. Antimicrobial action of TiO₂ nanoparticles was also shown to be higher against both (gram-negative and gram-positive) human pathogenic microorganisms. The biosynthesized nanoparticles demonstrated a greater zone of inhibitory activity against gram-positive (*B. subtilis*, *S. aureus*) pathogenic bacteria than gram-negative (*P. aeruginosa*, *E. coli*) in comparison of bare TiO₂ nanoparticles. Furthermore, we may conclude that these biosynthesized nanoparticles can be employed in medicine as therapeutic agents based on in vitro antibacterial activity against human pathogenic bacteria.

Author Contributions: A.A.: conceptualization, methodology, formal analysis, investigation, and writing—original draft preparation; V.U.S.: resources, writing—review and editing; W.U.R.: formal analysis, investigation; M.K.A.: formal analysis, investigation; W.A.S.: project administration, supervision; A.M.A.: funding acquisition, writing—review and editing; M.A.H.: funding acquisition, writing—review and editing; M.R.: funding acquisition, writing—review and editing. All authors have read and agreed to the published version of the manuscript.

Funding: This research was funded by Taif University Researchers Supporting Project number (TURSP-2020/244), Taif University, Taif, Saudi Arabia.

Data Availability Statement: Not applicable.

Acknowledgments: Authors are thankful to Taif University Researchers Supporting Project number (TURSP-2020/244), Taif University, Taif, Saudi Arabia. The author, A.A., gratefully acknowledges the financial assistance in terms of “non-NET fellowship” by University Grant Commission (UGC), New Delhi. Further, the authors are also grateful to the Central Instrumentation Facility (CIF) and Centre for Nanoscience and Nanotechnology, Jamia Millia Islamia, New Delhi for providing the experimental facility.

Conflicts of Interest: The authors declare no conflict of interest. The funders had no role in the designs of the study; in the collection, analyses, or interpretation of data; in the writing of the manuscript; or in the decision to publish the results.

References

1. Sharma, M.; Behl, K.; Nigam, S.; Joshi, M. TiO₂-GO nanocomposite for photocatalysis and environmental applications: A green synthesis approach. *Vacuum* **2018**, *156*, 434–439. [[CrossRef](#)]
2. Moritz, T.; Reiss, J.; Diesner, K.; Su, D.; Chemseddine, A. Nanostructured Crystalline TiO₂ through Growth Control and Stabilization of Intermediate Structural Building Units. *J. Phys. Chem. B* **1997**, *101*, 8052–8053. [[CrossRef](#)]
3. Ahmad, W.; Jaiswal, K.K.; Soni, S. Green synthesis of titanium dioxide (TiO₂) nanoparticles by using *Mentha arvensis* leaves extract and its antimicrobial properties. *Inorg. Nano-Metal. Chem.* **2020**, *50*, 1032–1038. [[CrossRef](#)]
4. Al-Shabib, N.A.; Husain, F.M.; Qais, F.A.; Ahmad, N.; Khan, A.; Alyousef, A.A.; Arshad, M.; Noor, S.; Khan, J.M.; Alam, P.; et al. Phyto-Mediated Synthesis of Porous Titanium Dioxide Nanoparticles From *Withania somnifera* Root Extract: Broad-Spectrum Attenuation of Biofilm and Cytotoxic Properties Against HepG2 Cell Lines. *Front. Microbiol.* **2020**, *11*, 1–13. [[CrossRef](#)] [[PubMed](#)]
5. Bekele, E.T.; Gonfa, B.A.; Zelekew, O.A.; Belay, H.H.; Sabir, F.K. Synthesis of Titanium Oxide Nanoparticles Using Root Extract of *Kniphofia foliosa* as a Template, Characterization, and Its Application on Drug Resistance Bacteria. *J. Nanomater.* **2020**, *2020*, 1–10. [[CrossRef](#)]
6. Rodríguez-González, V.; Terashima, C.; Fujishima, A. Applications of photocatalytic titanium dioxide-based nanomaterials in sustainable agriculture. *J. Photochem. Photobiol. C Photochem. Rev.* **2019**, *40*, 49–67. [[CrossRef](#)]
7. Khaled, J.M.; Alharbi, N.S.; Kadaikunnan, S.; Alobaidi, A.S.; Al-Anbr, M.N.; Gopinath, K.; Aurmugam, A.; Govindarajan, M.; Benelli, G. Green Synthesis of Ag Nanoparticles with Anti-bacterial Activity Using the Leaf Extract of an African Medicinal Plant, *Ipomoea asarifolia* (Convolvulaceae). *J. Clust. Sci.* **2017**, *28*, 3009–3019. [[CrossRef](#)]
8. Auffan, M.; Rose, J.; Bottero, J.-Y.; Lowry, G.V.; Jolivet, J.-P.; Wiesner, M.R. Towards a definition of inorganic nanoparticles from an environmental, health and safety perspective. *Nat. Nanotechnol.* **2009**, *4*, 634–641. [[CrossRef](#)]
9. Hunagund, S.M.; Desai, V.R.; Barretto, D.A.; Pujar, M.S.; Kadadevarmath, J.S.; Vootla, S.; Sidarai, A.H. Photocatalysis effect of a novel green synthesis gadolinium doped titanium dioxide nanoparticles on their biological activities. *J. Photochem. Photobiol. A Chem.* **2017**, *346*, 159–167. [[CrossRef](#)]
10. Zhang, Q.; Ma, L.; Shao, M.; Huang, J.; Ding, M.; Deng, X.; Wei, X.; Xu, X. Anodic Oxidation Synthesis of One-Dimensional TiO₂ Nanostructures for Photocatalytic and Field Emission Properties. *J. Nanomater.* **2014**, *2014*, 1–14. [[CrossRef](#)]

11. Jose, T.; Vincent, C.; Lilly, K.O.; Lazar, M.A. Selective photocatalytic dye degradation by surface charged TiO₂. *Mater. Today Proc.* **2019**, *9*, 21–26. [[CrossRef](#)]
12. Bui, D.; Pham, H.; Cao, T.; Pham, V. Preparation of conjugated polyvinyl chloride/TiO₂ nanotubes for Rhodamine B photocatalytic degradation under visible light. *J. Chem. Technol. Biotechnol.* **2020**, *95*, jctb.6466. [[CrossRef](#)]
13. Fang, C.-S.; Chen, Y.-W. Preparation of titania particles by thermal hydrolysis of TiCl₄ in n-propanol solution. *Mater. Chem. Phys.* **2003**, *78*, 739–745. [[CrossRef](#)]
14. Akurati, K.K.; Vital, A.; Fortunato, G.; Hany, R.; Nueesch, F.; Graule, T. Flame synthesis of TiO₂ nanoparticles with high photocatalytic activity. *Solid State Sci.* **2007**, *9*, 247–257. [[CrossRef](#)]
15. Chaisuk, C.; Wehatoranawee, A.; Preampiyawat, S.; Netiphat, S.; Shotipruk, A.; Mekasuwandumrong, O. Preparation and characterization of CeO₂/TiO₂ nanoparticles by flame spray pyrolysis. *Ceram. Int.* **2011**, *37*, 1459–1463. [[CrossRef](#)]
16. Ba-Abbad, M.M.; Kadhum, A.A.H.; Mohamad, A.B.; Takriff, M.S.; Sopian, K. Synthesis and catalytic activity of TiO₂ nanoparticles for photochemical oxidation of concentrated chlorophenols under direct solar radiation. *Int. J. Electrochem. Sci.* **2012**, *7*, 4871–4888.
17. Chen, S.F.; Li, J.P.; Qian, K.; Xu, W.P.; Lu, Y.; Huang, W.X.; Yu, S.H. Large scale photochemical synthesis of M@TiO₂ nanocomposites (M = Ag, Pd, Au, Pt) and their optical properties, CO oxidation performance, and antibacterial effect. *Nano Res.* **2010**, *3*, 244–255. [[CrossRef](#)]
18. Khade, G.V.; Suwarnkar, M.B.; Gavade, N.L.; Garadkar, K.M. Green synthesis of TiO₂ and its photocatalytic activity. *J. Mater. Sci. Mater. Electron.* **2015**, *26*, 3309–3315. [[CrossRef](#)]
19. Santhoshkumar, T.; Rahuman, A.A.; Jayaseelan, C.; Rajakumar, G.; Marimuthu, S.; Kirthi, A.V.; Velayutham, K.; Thomas, J.; Venkatesan, J.; Kim, S.-K. Green synthesis of titanium dioxide nanoparticles using Psidium guajava extract and its antibacterial and antioxidant properties. *Asian Pac. J. Trop. Med.* **2014**, *7*, 968–976. [[CrossRef](#)]
20. Duan, H.; Wang, D.; Li, Y. Green chemistry for nanoparticle synthesis. *Chem. Soc. Rev.* **2015**, *44*, 5778–5792. [[CrossRef](#)]
21. Weir, A.; Westerhoff, P.; Fabricius, L.; Hristovski, K.; von Goetz, N. Titanium Dioxide Nanoparticles in Food and Personal Care Products. *Environ. Sci. Technol.* **2012**, *46*, 2242–2250. [[CrossRef](#)] [[PubMed](#)]
22. Zeman, P.; Takabayashi, S. Nano-scaled photocatalytic TiO₂ thin films prepared by magnetron sputtering. *Thin Solid Film.* **2003**, *433*, 57–62. [[CrossRef](#)]
23. Sharma, J.K.; Srivastava, P.; Ameen, S.; Akhtar, M.S.; Sengupta, S.K.; Singh, G. Phytoconstituents assisted green synthesis of cerium oxide nanoparticles for thermal decomposition and dye remediation. *Mater. Res. Bull.* **2017**, *91*, 98–107. [[CrossRef](#)]
24. Kweinor Tetteh, E.; Rathilal, S. Adsorption and Photocatalytic Mineralization of Bromophenol Blue Dye with TiO₂ Modified with Clinoptilolite/Activated Carbon. *Catalysts* **2020**, *11*, 7. [[CrossRef](#)]
25. Sharma, V.; Sharma, R.; Gautam, D.; Kuca, K.; Nepovimova, E.; Martins, N. Role of Vacha (*Acorus calamus* Linn.) in Neurological and Metabolic Disorders: Evidence from Ethnopharmacology, Phytochemistry, Pharmacology and Clinical Study. *J. Clin. Med.* **2020**, *9*, 1176. [[CrossRef](#)]
26. Mukherjee, P.K.; Kumar, V.; Mal, M.; Houghton, P.J. *Acorus calamus*: Scientific Validation of Ayurvedic Tradition from Natural Resources. *Pharm. Biol.* **2007**, *45*, 651–666. [[CrossRef](#)]
27. Nair, A.; Chattopadhyay, D.; Saha, B. Plant-Derived Immunomodulators. In *New Look to Phytomedicine*; Elsevier: Amsterdam, The Netherlands, 2019; pp. 435–499. ISBN 9780128146200.
28. Li, X.; Robinson, S.M.; Gupta, A.; Saha, K.; Jiang, Z.; Moyano, D.F.; Sahar, A.; Riley, M.A.; Rotello, V.M. Functional Gold Nanoparticles as Potent Antimicrobial Agents against Multi-Drug-Resistant Bacteria. *ACS Nano* **2014**, *8*, 10682–10686. [[CrossRef](#)]
29. Brown, A.N.; Smith, K.; Samuels, T.A.; Lu, J.; Obare, S.O.; Scott, M.E. Nanoparticles Functionalized with Ampicillin Destroy Multiple-Antibiotic-Resistant Isolates of *Pseudomonas aeruginosa* and Enterobacter aerogenes and Methicillin-Resistant *Staphylococcus aureus*. *Appl. Environ. Microbiol.* **2012**, *78*, 2768–2774. [[CrossRef](#)]
30. Makuła, P.; Pacia, M.; Macyk, W. How To Correctly Determine the Band Gap Energy of Modified Semiconductor Photocatalysts Based on UV–Vis Spectra. *J. Phys. Chem. Lett.* **2018**, *9*, 6814–6817. [[CrossRef](#)]
31. Thakur, B.K.; Kumar, A.; Kumar, D. Green synthesis of titanium dioxide nanoparticles using *Azadirachta indica* leaf extract and evaluation of their antibacterial activity. *S. Afr. J. Bot.* **2019**, *124*, 223–227. [[CrossRef](#)]
32. Saranya, K.S.; Vellora Thekkae Padil, V.; Senan, C.; Pilankatta, R.; Saranya, K.; George, B.; Waclawek, S.; Černík, M. Green Synthesis of High Temperature Stable Anatase Titanium Dioxide Nanoparticles Using Gum Kondagogu: Characterization and Solar Driven Photocatalytic Degradation of Organic Dye. *Nanomaterials* **2018**, *8*, 1002. [[CrossRef](#)] [[PubMed](#)]
33. Vijayalakshmi, U.; Chellappa, M.; Anjaneyulu, U.; Manivasagam, G. Preparation and evaluation of the cytotoxic nature of TiO₂ nanoparticles by direct contact method. *Int. J. Nanomed.* **2015**, *10*, 31. [[CrossRef](#)]
34. Sankar, R.; Rizwana, K.; Shivashangari, K.S.; Ravikumar, V. Ultra-rapid photocatalytic activity of *Azadirachta indica* engineered colloidal titanium dioxide nanoparticles. *Appl. Nanosci.* **2015**, *5*, 731–736. [[CrossRef](#)]
35. Hurum, D.C.; Agrios, A.G.; Gray, K.A.; Rajh, T.; Thurnauer, M.C. Explaining the Enhanced Photocatalytic Activity of Degussa P25 Mixed-Phase TiO₂ Using EPR. *J. Phys. Chem. B* **2003**, *107*, 4545–4549. [[CrossRef](#)]
36. Sonker, R.K.; Hitkari, G.; Sabhajeet, S.R.; Sikarwar, S.; Rahul, Singh, S. Green synthesis of TiO₂ nanosheet by chemical method for the removal of Rhodamin B from industrial waste. *Mater. Sci. Eng. B* **2020**, *258*, 114577. [[CrossRef](#)]
37. Le, T.T.T.; Tran, T.D. Photocatalytic Degradation of Rhodamine B by C and N Codoped TiO₂ Nanoparticles under Visible-Light Irradiation. *J. Chem.* **2020**, *2020*, 1–8. [[CrossRef](#)]

38. Zhu, J.; Zhang, J.; Chen, F.; Iino, K.; Anpo, M. High activity TiO₂ Photocatalysts Prepared by a Modified Sol–gel Method: Characterization and their Photocatalytic Activity for the Degradation of XRG and X-GL. *Top. Catal.* **2005**, *35*, 261–268. [[CrossRef](#)]
39. Ramimoghadam, D.; Bagheri, S.; Abd Hamid, S.B. Biotemplated Synthesis of Anatase Titanium Dioxide Nanoparticles via Lignocellulosic Waste Material. *Biomed. Res. Int.* **2014**, *2014*, 1–7. [[CrossRef](#)]
40. He, J.; Du, Y.; Bai, Y.; An, J.; Cai, X.; Chen, Y.; Wang, P.; Yang, X.; Feng, Q. Facile Formation of Anatase/Rutile TiO₂ Nanocomposites with Enhanced Photocatalytic Activity. *Molecules* **2019**, *24*, 2996. [[CrossRef](#)]
41. Dror, I.; Fink, L.; Weiner, L.; Berkowitz, B. Elucidating the catalytic degradation of enrofloxacin by copper oxide nanoparticles through the identification of the reactive oxygen species. *Chemosphere* **2020**, *258*, 127266. [[CrossRef](#)]
42. Ansari, M.S.; Raees, K.; Ali Khan, M.; Rafiquee, M.Z.A.; Otero, M. Kinetic Studies on the Catalytic Degradation of Rhodamine B by Hydrogen Peroxide: Effect of Surfactant Coated and Non-Coated Iron (III) Oxide Nanoparticles. *Polymers* **2020**, *12*, 2246. [[CrossRef](#)] [[PubMed](#)]
43. Thao, N.T.; Nga, H.T.P.; Vo, N.Q.; Nguyen, H.D.K. Advanced oxidation of rhodamine B with hydrogen peroxide over Zn Cr layered double hydroxide catalysts. *J. Sci. Adv. Mater. Devices* **2017**, *2*, 317–325. [[CrossRef](#)]
44. Wang, S.; Jia, Y.; Song, L.; Zhang, H. Decolorization and Mineralization of Rhodamine B in Aqueous Solution with a Triple System of Cerium(IV)/H₂O₂/Hydroxylamine. *ACS Omega* **2018**, *3*, 18456–18465. [[CrossRef](#)] [[PubMed](#)]
45. Ali, S.; Tanweer, M.S.; Alam, M. Kinetic, isothermal, thermodynamic and adsorption studies on Mentha piperita using ICP-OES. *Surf. Interfaces* **2020**, *19*, 100516. [[CrossRef](#)]
46. Alshammari, A.; Bagabas, A.; Assulami, M. Photodegradation of rhodamine B over semiconductor supported gold nanoparticles: The effect of semiconductor support identity. *Arab. J. Chem.* **2019**, *12*, 1406–1412. [[CrossRef](#)]
47. Azizi-Lalabadi, M.; Ehsani, A.; Divband, B.; Alizadeh-Sani, M. Antimicrobial activity of Titanium dioxide and Zinc oxide nanoparticles supported in 4A zeolite and evaluation the morphological characteristic. *Sci. Rep.* **2019**, *9*, 17439. [[CrossRef](#)]
48. Chawla, V.; Sathaye, S. Biosynthesis of silver nanoparticles using methanolic extracts of Acorus calamus, and assessment of its antioxidant and antimicrobial activity. *J. Med. Plants Stud.* **2017**, *5*, 358–363.
49. Ganesan, R.; Gurumalles Prabu, H. Synthesis of gold nanoparticles using herbal Acorus calamus rhizome extract and coating on cotton fabric for antibacterial and UV blocking applications. *Arab. J. Chem.* **2019**, *12*, 2166–2174. [[CrossRef](#)]
50. Dubey, R.S.; Krishnamurthy, K.V.; Singh, S. Experimental studies of TiO₂ nanoparticles synthesized by solgel and solvothermal routes for DSSCs application. *Results Phys.* **2019**, *14*, 102390. [[CrossRef](#)]
51. Natarajan, K.; Natarajan, T.S.; Bajaj, H.C.; Tayade, R.J. Photocatalytic reactor based on UV-LED/TiO₂ coated quartz tube for degradation of dyes. *Chem. Eng. J.* **2011**, *178*, 40–49. [[CrossRef](#)]
52. Tayade, R.J.; Natarajan, T.S.; Bajaj, H.C. Photocatalytic Degradation of Methylene Blue Dye Using Ultraviolet Light Emitting Diodes. *Ind. Eng. Chem. Res.* **2009**, *48*, 10262–10267. [[CrossRef](#)]
53. Ahmad, S.; Siddiqui, V.U.; Ansari, A.; Siddiqi, W.A.; Akram, M.K. Effective photocatalytic activity of graphene/polyindole nanocomposites to degrade the herbicide 2,4-dichlorophenoxyacetic acid (2,4-D) for water treatment. In Proceedings of the AIP Conference Proceedings, New Delhi, India, October 2020; 2276, p. 020016.
54. Siddiqui, V.; Ansari, A.; Ansari, M.; Akram, M.; Siddiqi, W.; Alosaimi, A.; Hussein, M.; Rafatullah, M. Optimization of Facile Synthesized ZnO/CuO Nanophotocatalyst for Organic Dye Degradation by Visible Light Irradiation Using Response Surface Methodology. *Catalysts* **2021**, *11*, 1509. [[CrossRef](#)]
55. AlOthman, Z.A.; Badjah, A.Y.; Alharbi, O.M.L.; Ali, I. Synthesis of chitosan composite iron nanoparticles for removal of diclofenac sodium drug residue in water. *Int. J. Biol. Macromol.* **2020**, *159*, 870–876. [[CrossRef](#)] [[PubMed](#)]
56. Bauer, A.W.; Kirby, W.M.; Sherris, J.C.; Turck, M. Antibiotic susceptibility testing by a standardized single disk method. *Am. J. Clin. Pathol.* **1966**, *45*, 493–496. [[CrossRef](#)]